Journal of Hydroscience and Hydraulic Engineering
Vol. 5, No. 2, February, 1988, pp.25-37

NUMERICAL MODELING OF A THERMAL DISCHARGE HEAT TRANSPORT IN THE TRANSITION REGION

By

S.K.W. Tou

Nanyang Technological Institute, Singapore

and

K Arumugam

The City University, London, U.K.

SYNOPSIS

A vertically integrated thermal-hydraulic model is developed based on the finite element Lax-Wendroff method to study the heat transport phenomenon in the transition region. In addition to the advection-diffusion heat transport, the effects of thermal-hydraulic interaction and surface heat exchange are included in the model. The numerical results show a fair degree of agreement with those obtained from a physical model. The temperature in the transition region varies roughly between 50% and 15% of the maximum temperature rise at the effluent discharge point. This region appears to lie between radii of 0.4 km and 0.8 km under the assumed operating conditions. The reasons for using lumped mass formulation in dynamic problems are investigated both from the mathematical and physical point of view. The method is efficient and reduces computer core storage. It also permits the use of larger elements as compared to the method of consistent mass representation.

INTRODUCTION

Hydraulic laboratories all over the world have been increasingly involved in combined physical and mathematical modeling of thermal-hydraulic problems. Physical model studies are valuable tools for demonstrating the characteristics of a phenomenon and for deriving solutions to problems that do not lend themselves to analytical computation. Computational analysis is commended for efficient solutions of two-dimensional problems. Numerical models are limited in space towards the lower end of the scale whereas physical models are limited towards the upper end. Therefore numerical models are usually more suitable for simulation of large-scale thermal-hydraulic processes in the transition or far field, whereas physical models are more suitable for investigation of local phenomena of relatively small scale. It is often found that a combination of methods benefits for each other and may result in more efficient approach to the required solutions. The present paper presents a combined model study of the heat transport of a thermal discharge in the transition region.

FLOW REGIME IDENTIFICATION

When a heated jet discharges into an unstratified receiving water, the initial stage of vertical mixing is transient and may not be considered in long-term prediction. It is followed by further cooling in the form of horizontal diffusion and dispersion as well as heat loss to the atmosphere. The horizontal mixing processes last relatively longer. It requires some distance before the waste heat can be distributed across the flow in the form of a belt. The temperature distribution downstream from the point of a thermal discharge is primarily determined by the hydrodynamic characteristics of the stream and the meteorological conditions prevailing at the site. The heat transport phenomenon of a thermal discharge in nature is extremely complicated and is affected by numerous factors. From an analytical stand point, the phenomenon could be viewed macroscopically as taking place in three regions, viz., the near field, the transition region and the far field. Figures 1 and 2 depict the general development of a thermal discharge in these three regions. The prediction of temperature and flow distribution in these three regions requires an understanding of the various mechanisms in the heat transport processes individually and collectively.

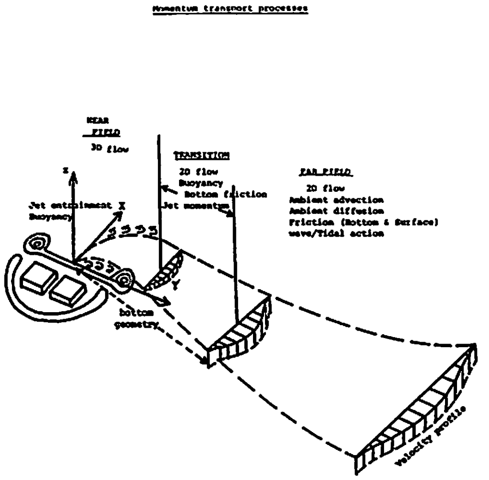

Figure 1 ·· Hydrodynamics of a thermal discharge

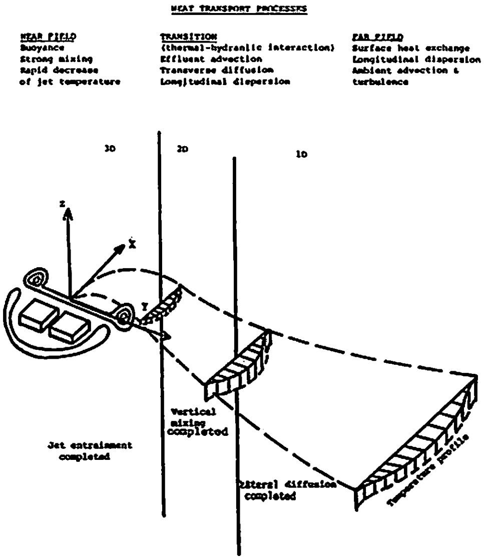

Figure 2 Thermodynamics of the discharge

DYNAMICS OF TRANSITION REGION

Outside the near field and covering a much wider area is the transition region. This transition region must be employed to allow the heated effluent to approach hydrostatic equilibrium and to allow the longitudinal velocity to approach the velocity in the far field. Beyond the transition region, the far field model can then assume a velocity independent of the discharge in the near field and decouple the momentum and the energy equations. The concept of heat conservation in the transition region can be used as a rough approximation to the true physical situation and can provide the basic linkage for the near and far fields [7]. In practice, this region is of great importance because the excess temperature is still significant and a large area is affected. Unfortunately, it has received little attention and no firm theories have yet been advanced for this transition region to integrate the near and far field analysis. A complete picture of the temperature distribution in the near and far fields necessitates the implementation of a transition model and entails the development of a theory for this transition region [8].

There is no clear-cut physical boundary between different zones. The boundary between the near field and the transition zone is defined as where the discharge has reached the point when its jet-like behaviour ceases and the action of turbulent entrainment has completed. To this end, the three-dimensional temperature and flow fields could be reduced to two-dimensional approximation as the vertical mixing is complete and the flow and heat transport are essentially horizontal. The jet velocity is also reduced to a velocity comparable with that in the transition region. In this region, the effluent is still spreading laterally and longitudinally due to thermal-hydraulic interaction and initial momentum respectively. Further out, as the temperature and the velocity profiles become uniform laterally, density-induced spreading diminishes. This marks the outer boundary between the transition region and the far field. The extent of each region depends on the thermal-hydraulics of the discharge, the outlet design, the bottom topography, the ambient conditions and other factors. From the momentum considerations, Adams showed that the radius of the transition region varies from 0.4 km to 0.8 km [1].

NUMERICAL MODEL FORMULATION

Governing Equations

The governing equations for the thermal-hydraulic model consist of the vertically integrated shallow water equations and the advection-diffusion equation. They are given below [6, 10]:

The momentum equations

$$\frac{\partial U}{\partial t} + \frac{U\partial U}{\partial x} + \frac{V\partial U}{\partial y} + \frac{g\partial \xi}{\partial x} + \frac{\beta g H\ \partial \Delta T}{\rho_\infty\ \partial x} + \frac{K_b\sqrt{U^2 + V^2}\ U - fV}{H} = 0 \qquad (1)$$

$$\frac{\partial V}{\partial t} + \frac{V\partial V}{\partial y} + \frac{U\partial V}{\partial x} + \frac{g\partial \xi}{\partial y} + \frac{\beta g H\partial \Delta T}{\rho_\infty \partial y} + \frac{K_b\sqrt{U^2 + V^2}\ V + fU}{H} = 0 \qquad (2)$$

The continuity equation

$$\frac{\partial \xi}{\partial t} + \frac{\partial UH}{\partial x} + \frac{\partial VH}{\partial y} = 0 \qquad (3)$$

The advection-diffusion equation

$$\frac{\partial(\Delta TH)}{\partial t} + \frac{\partial(U\ \Delta TH)}{\partial x} + \frac{\partial(V\ \Delta TH)}{\partial y} = \frac{\partial(K_x H}{\partial x}\ \frac{\partial \Delta T)}{\partial\ x} + \frac{\partial(K_y H}{\partial y}\ \frac{\partial \Delta T)}{\partial\ y} + \frac{\phi \Delta T}{C_p \rho} \qquad (4)$$

Initial/Boundary Conditions

In order to solve the above governing equations, the following initial/boundary conditons need to be specified.

$U = 0$

$V = 0$

$\xi = 0$

$\Delta T = 0$ at boundary C_1 (Figure 4)

No flux of matter is allowed at the water-land boundary, i.e.,

$(U,V)\cdot\bar{n} = 0$ at C_2 (Figure 4)

The steady velocity and temperature at the discharge point are specified as follows:

$U = U^*$

$V = V^*$

$\Delta T = \Delta T^*$

When there is no heat transfer across the solid boundary, the heat flux normal to the boundary is:

$$\frac{\partial \Delta T}{\partial n} = 0 \quad \text{at } C_2$$

For cold start, the initial conditions are:

$U = 0$

$V = 0$

$\xi = 0$

and $\Delta T = 0$

Finite Element Discretization

The finite element method plays a key role in transforming the governing equations into a numerical procedure. It assumes that the flow and temperature fields can be analysed by dividing them spatially into small domains which can be represented as follows:

$$U = [\ N\ ]^e \{U\}^e \tag{5}$$

$$V = [\ N\ ]^e \{V\}^e \tag{6}$$

$$\xi = [\ N\ ]^e \{\xi\}^e \tag{7}$$

$$\Delta T = [\ N\ ]^e \{\Delta T\}^e \tag{8}$$

In order to select an interpolation function $[\ N\ ]^e$, it is necessary to consider its relationship with the discretization procedure for the time function. In tidal flow computation, the modified two-step Lax-Wendroff scheme has been successfully applied to a triangular element with three nodes by using a linear polynomial function in space [3, 4]. For the heat transport computation, the same linear polynomial function is employed for the temperature field, such that:

$$N_i^e = a_i + b_i x + c_i y \tag{9}$$

$i = 1, 2, 3$

The coefficients a_i, b_i and c_i are determined by the coordinates of the node of the triangular element. In the present model, it is also assumed that the same interpolation function is used to approximate the time rate change of variables, i.e.,

$$\partial U/\partial t = [\ N\ ]^e \partial\{U\}^e/\partial t \tag{10}$$

$$\partial V/\partial t = [\ N\ ]^e \partial\{V\}^e/\partial t \tag{11}$$

$$\partial \xi/\partial t = [\ N\ ]^e \partial\{\xi\}^e/\partial t \tag{12}$$

and $$\partial \Delta T/\partial t = [\ N\ ]^e \partial\{\Delta T\}^e/\partial t \tag{13}$$

The Galerkin integral for equation (1), (2), (3) or (4) is given as follows:

$$\sum_{e=1}^{E} \int_{\Omega} N_i^e\{L([N]^e\{U\}^e,\ [N]^e\{V\}^e,\ [N]^e\{\xi\}^e,\ [N]^e\{\Delta T\}^e)-F^e\}d\Omega = 0 \quad (14)$$

where L = differential operator

F^e= the sum of all terms not containing U, V, ξ or ΔT

and i = 1, 2, 3, 4......M

Integrating by parts yields,

$$\sum_{e=1}^{E} m_{ij}^e \partial U_j^e/\partial t = -\sum_{e=1}^{E}\{(b_j U_j^e)(m_{ij}^e U_j^e) + (c_j U_j^e)(m_{ij}^e V_j^e)\}/(2\Delta)$$

$$-\sum_{e=1}^{E} K_b \psi_\Omega m_{ij}^e U_j^e + \sum_{e=1}^{E} f\ m_{ij}^e V_j^e + \sum_{e=1}^{E} \beta\ g\ H_\Omega q_i^e (b_j\ \Delta T_j^e)/(2\Delta\rho_\Omega)$$

$$-\sum_{e=1}^{E} g\ q_i^e b_j \xi_j^e/(2\Delta) \quad (15)$$

$$\sum_{e=1}^{E} m_{ij}^e \partial V_j^e/\partial t = -\sum_{e=1}^{E}\{(c_j V_j^e)(m_{ij}^e V_j^e) + (b_j V_j^e)(m_{ij}^e U_j^e)\}/(2\Delta)$$

$$-\sum_{e=1}^{E} K_b \psi_\Omega m_{ij}^e V_j^e - \sum_{e=1}^{E} f m_{ij}^e U_j^e + \sum_{e=1}^{E} \beta\ g\ H_\Omega q_i^e (c_j \Delta T_j^e)/(2\Delta\rho_\Omega)$$

$$-\sum_{e=1}^{E} g\ q_i^e (c_j \xi_j^e)/(2\Delta) \quad (16)$$

$$\sum_{e=1}^{E} m_{ij}^e \partial \xi_j^e/\partial t = -\sum_{e=1}^{E}\{q_i^e (b_j U_j^e) + q_i^e\ (c_j V_j^e)\}H_\Omega/(2\Delta) \quad (17)$$

$$\sum_{e=1}^{E} m_{ij}^e \partial \Delta T_j^e/\partial t = -\sum_{e=1}^{E}\{(b_j \Delta T_j^e)(m_{ij}^e U_j^e) + (b_j U_j^e)(m_{ij}^e \Delta T_j^e)$$

$$+ (c_j V_j^e)(m_{ij}^e\ \Delta T_j^e) + (c_j \Delta T_j^e)(m_{ij}^e V_j^e)$$

$$+ K_x(b_i b_j \Delta T_j^e)/2 + K_y(c_i c_j \Delta T_j^e)/2\ \}\ /(2\Delta)$$

$$+\sum_{e=1}^{E} m_{ij}^e \Delta T_j^e \phi/(\rho_\Omega C_p H_\Omega) \quad (18)$$

where $$m_{ij}^e = \int_\Omega N_i^e N_j^e d\ \Omega \quad (19)$$

$$= \begin{cases} \Delta/6 & \text{for } i = j \\ \Delta/12 & \text{for } i \neq j \end{cases}$$

$$q_i^e = \int_\Omega N_i^e d\ \Omega$$

$$= \Delta/3$$

$$H\Omega = 1/3 \sum_{j=1}^{3} H_j^e$$

$$\psi\Omega = \sqrt{(1/3\sum_{j=1}^{3} U_j^e)^2 + (1/3\sum_{j=1}^{3} V_j^e)^2/H_\Omega}$$

$$K_b = g/(H_\Omega^{1/6}/\lambda)^2$$

$$\rho_\Omega = \rho_\infty - \beta/3 \sum_{j=1}^{3}\Delta T_j^e$$

$i = 1, 2, 3$

and $j = 1, 2, 3$

Note that indicial summation is implied in the above equations.

The above discretization procedure introduces a change in the nature of the problem as the domain with infinite degrees of freedom is approximated by a discrete domain with finite degrees of freedom. Equations (15), (16), (17) and (18) apply only at each node after the domain is discretized whereas equations (1), (2), (3) and (4) hold everywhere within the domain. The accuracy of the solution for the discretized domain depends on the scheme used to transform equations (1), (2), (3) and (4) into the discrete form given by equations (15), (16), (17) and (18) respectively. In addition, the choice of mass matrix m_{ij}^e is also critical in dynamic analysis if reliable and accurate results are to be obtained [2].

Lumped Masses versus Consistent Masses

Because the same interpolation function is used for the time rate of change of variables, the matrix m_{ij}^e expressed by equation (19) is a consistent mass matrix. This matrix is usually a full matrix. The resulting assemblage mass matrix $\sum_{e=1}^{E} m_{ij}^e$ is also a non-diagonal matrix. Suppose an arbitrary element $\sum_{e=1}^{E} m_{ij}^e$ $(i \neq j)$ is a non-zero element in the left hand side of equation (15). This element consists of $\partial U_i/\partial t$ and $\partial U_j/\partial t$ during the process of assemblage. This means that the ith equation in the assemblage equation (15) includes terms $\partial U_j/\partial t$ coming from the jth node. There is contradiction in the ith equation resulting from the corresponding ith node. This is because equation (15) requires that the resultant external force at the ith node must be taken as the sum of all the external forces at that node. This resultant external force should not be affected by the external forces at any other nodes. The same analysis applies to equations (16), (17) and (18).

To resolve the above dilemma, an alternative is to employ lumped mass matrix which assumes that all the mass tributary to a particular node is concentrated at the node. The lumped mass matrix for a triangular element is [2]:

$$\overset{*}{m}{}_{ij}^{e} = \begin{cases} \Delta/3 & \text{for } i = j \\ 0 & \text{for } i \neq j \end{cases} \tag{20}$$

The above lumped mass matrix is independent of the interpolation function being used and is diagonal. The resulting assemblage mass matrix $\sum_{e=1}^{E} \overset{*}{m}{}_{ij}^{e}$ is also diagonal . In this case, the ith equation derived at the ith node will not be affected by the jth node as the element $\sum_{e=1}^{E} \overset{*}{m}{}_{ij}^{e}$ $(i \neq j)$ now assumes zero value.

The result by using lumped mass representation is indeed consistent with that of equation (15, (16), (17) or (18). However, the requirement of continuity in $\partial U/\partial t$ within the element is abandoned. This is physically justified as the inertia force of an element in dynamic analysis is the sum of the inertia forces of the lumped masses at the nodes regardless of the force distribution within the element. The lumped masses will not cause inertia forces to act on any other lumped masses except at its own node.

Based on the above analysis, it can be seen that the lumped mass representation should be used in dynamic problems in order to obtain reliable results. The advantages of using lumped mass formulation are that it simplifies the computation and reduces computer core storage. In comparison with the consistent mass representation, the lumped mass does not depend on the interpolation function and element nodal locations. Hence, larger elements can be employed.

Finite Difference Time Discretization

The time integration scheme adopted in the present model is the modified two-step Lax-Wendroff scheme which is an extension of the well known Runge-Kutta method. This integration scheme is first introduced by Kawahara in the study of tsunami wave propagation. It requires that the total time be segmented into equal time interval Δt, i.e.,

$$T = n\Delta t \qquad \text{for } n = 0,\ 1,\ 2,\ 3,\ \ldots\ldots,\ T/\Delta t$$

Let

$$W^e = \{ U_1^e,\ U_2^e,\ U_3^e \}^T$$

$$= \{ V_1^e,\ V_2^e,\ V_3^e \}^T$$

$$= \{ \xi_1^e,\ \xi_2^e,\ \xi_3^e \}^T$$

or

$$= \{ \Delta T_1^e,\ \Delta T_2^e,\ \Delta T_3^e \}^T$$

be the unknowns at the element nodes. Denoting their values at the nth time step as W_n^e, the explicit integration scheme advances the solution from time level n to time level n+1 in two steps. The first step advances the solution to an intermediate level $n+1/2$ as follows:

Step 1: At $(n,\ n+1/2)$, the forward difference yields

$$\sum_{e=1}^{E} \overset{*}{m}{}_{ij}^{e}\, W^e_{n+1/2} = \sum_{e=1}^{E} \bar{m}_{ij}^{e}\, W_n^e + \sum_{e=1}^{E} \Delta t/2\ G_n^e \tag{21}$$

Step 2: At $(n,\ n+1)$, the central difference gives

$$\sum_{e=1}^{E} \overset{*}{m}{}_{ij}^{e}\, W^e_{n+1} = \sum_{e=1}^{E} \bar{m}_{ij}^{e}\, W_n^e + \sum_{e=1}^{E} \Delta t\ G^e_{n+1/2} \tag{22}$$

where G^e = the sum of all terms excluding the time derivatives

$$\bar{m}_{ij}^{e} = \alpha\, \overset{*}{m}{}_{ij}^{e} + (1 - \alpha)\, m_{ij}^{e} \tag{23}$$

and $0 \leqq \alpha \leqq 1$ is the artificial damping coefficient. The stability criterion for this explicit time integration scheme can be determined according to the following equation [3, 4]:

$$\Delta t < \{(2-\alpha)/(3\sqrt{2})\}\,\{\Delta s/\sqrt{gH_{\Omega}}\} \tag{24}$$

In the present model, the time step Δt and α are taken as 4.5 seconds and 0.85 respectively.

Element Mesh Configuration

The element mesh configuration is determined by the model objectives as well as the required accuracy in the numerical simulation and the measurement of various parameters. The present model area is shown in Figure 3. It covers an area of 6.25 km² over which a total of 233 triangular elements are used. The corresponding mesh system is shown in Figure 4. The length of the element is kept small to reduce the numerical dispersion effect. The smallest elements whose sides are 85m are densely packed near the outlet as the velocity and temperature gradients are steep there. Large elements are placed where the gradients become small.

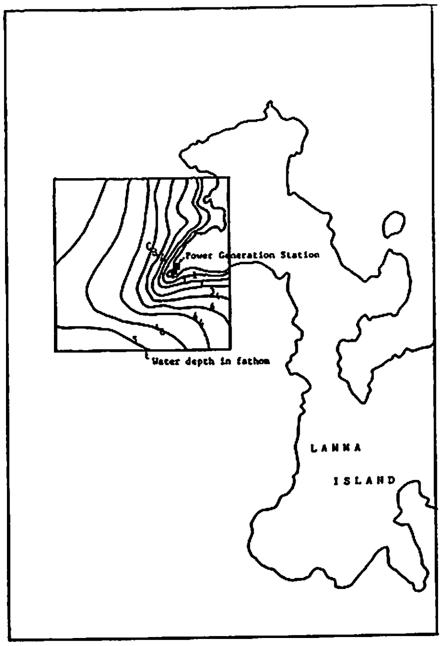

Figure 3 Location of Lamma Island Power Station (Hong Kong) and the Salient Points

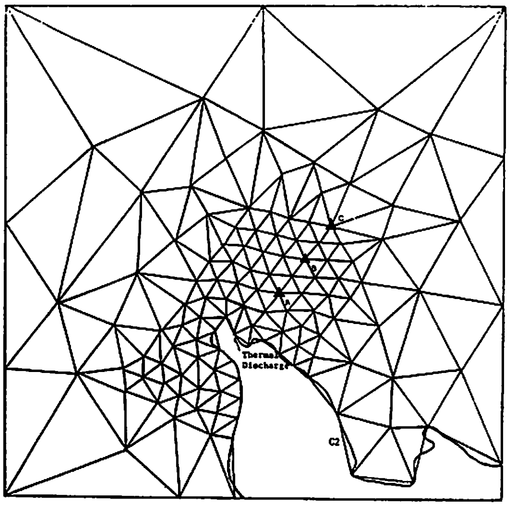

Figure 4
Mesh Configuration and Location of Salient Points

Scale 1 cm
= .125 Km

MODEL PARAMETERS AND SENSITIVITY TEST

The numerical model requires an estimate of the values of the overall thermal diffusivity, the surface heat exchange coefficient and the Manning roughness coefficient for the particular situation of concern. Unlike the molecular diffusivity, the overall thermal diffusivity is not a physical parameter of the fluid. It is a complicated function of the stream turbulence, width to depth ratio, bottom topography and, to a large extent, depends on the environment [5, 6, 9]. Like the momentum diffusivity, it cannot be determined by means of purely mathematical treatment. Taylor suggested to express it in terms of the statistical properties of turbulence. While our understanding of the detail mechanism is as incomplete as it is at present, the overall thermal diffusivity is one of the model parameters that have to be inferred from observations of related bulk stream variables. Great difficulties have arisen in interpreting the published values of coefficients of diffusivity as there are several ways of formulating the coefficients from the measured data. Despite the existence of many different formulation, the concept as such continues to be useful and practical in solving the transport problems. A survey of the literatures reveals that there is huge scatter of data regarding the coefficients of diffusivity ranging from 5×10^{-2} to 4×10^{4} m²/s [5, 9]. Rich [5] indicated that the diffusivity is greatly influenced by the natural environment. The data collected by Rich [5] and Pearson [9] provide useful information to estimate the diffusivity for a particular environment. As an initial estimate, the data suggested a mean diffusivity of 1 m²/s for a horizontal surface water environment [5]. Considering the fact that the lateral diffusivity is of the same order of magnitude as the longtudinal counterpart in the transition region, the following values are considered to be adequate for the numerical model:

$$K_x = 40 \text{ m}^2/\text{s}$$

$$K_y = 20 \text{ m}^2/\text{s}$$

The Peclet number then assumes the following values based on the mean discharge velocity and mean water depth in the prototype.

$$Pe_x = 0.61$$

$$Pe_y = 1.23$$

This indicates that both the advective transport and diffusive transport are dominant in the transition region and that the actual phenomenon is reasonably simulated. The surface heat exchange coefficient and Manning roughness coefficient are taken to be 0.15 kW/m²°C and 0.03 respectively in the numerical model.

The influence of the above parameters in affecting the behavior of the thermal plume may be assessed by systematic variation of each parameter. Initially the model is run with K_x ranging in magnitude from 0 to 500 m²/s while the rest are kept constant. The same test is repeated for K_y. The results indicate that the temperature rise in the transition region is sensitive to variation in the thermal diffusivity. The test on the surface heat exchange coefficient shows that the temperature distributions near the outer boundary are affected moderately by this parameter. Variation in this parameter is less influential in the transition region.

After several test runs, it is found that the Manning roughness coefficient is not a critical parameter in affecting the solution stability. This is because the solution stability for the present explicit integration scheme is governed by equation (24).

PHYSICAL MODEL

To demonstrate the prediction ability of the numerical model, a physical model is designed and constructed to simulate the thermal plume. The physical model has the following scales:

$$L_x = L_y$$

$$= 250$$

$$L_z = 50$$

The model distortion ration is 5. The use of a distorted model is justified provided that the flow and heat transport are two-dimensional in the model region of interest. Screens are introduced near the discharge to enhance the vertical mixing actions to completion before entering the model region. Water is used as the flow medium and the mean water depth is maintained at 0.14 m. The background water temperature is found to increase slightly after each test run. As an average, this temperature is taken to be 18°C. The model Reynolds number is 6.9×10^4. Turbulent flow is therefore reproduced in the model.

The model similitude is based on the densimetric Froude number, such that:

$$(Fr_\rho)_m = (Fr_\rho)_p \tag{27}$$

This leads to,

$$(Fr)_m = (Fr)_p \tag{28}$$

and $$(\sqrt{\Delta\rho / \rho_\infty})_m = (\sqrt{\Delta\rho / \rho_\infty})_p \tag{29}$$

The subscripts m and p denote the model and prototype respectively. Table 1 summarizes the assumed operating conditions for the prototype. The operating conditions for the physical model are determined by equations (25), (26), (28) and (29). They are also given in Table 1.

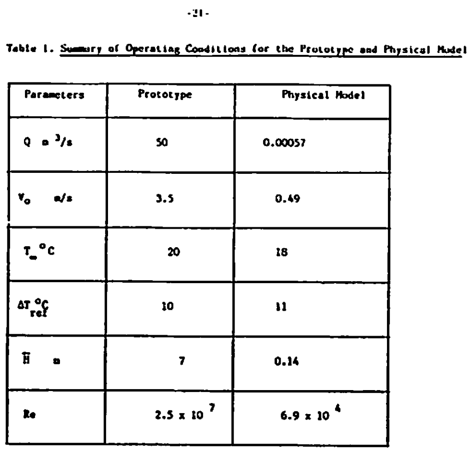

-21-

Table 1. Summary of Operating Conditions for the Prototype and Physical Model

Parameters	Prototype	Physical Model
Q m ^{3}/s	50	0.00057
V_o m/s	3.5	0.49
T_∞ °C	20	18
ΔT_{ref} °C	10	11
$\bar{H}$ m	7	0.14
Re	2.5×10^7	6.9×10^4

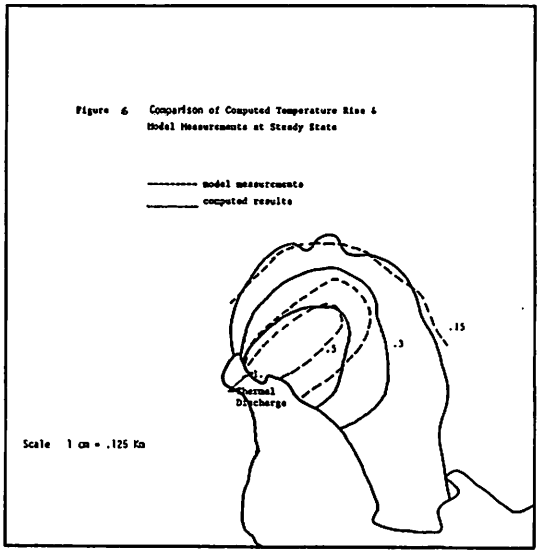

Figure 6 Comparison of Computed Temperature Rise & Model Measurements at Steady State

MODEL PERFORMANCE

The time history of computed temperature rise at various salient points is shown in Figure 5. The locations of these salient points are marked in Figure 4. The results show that the initial transient is damped out very quickly and a steady state is reached after approximately 0.5 hour. Figure 6 shows that the temperature in the transition region varies roughly between 50% and 15% of the maximum temperature rise at the discharge point. The transition region lies approximately between the radii of 0.4 km and 0.8 km for the assumed operating conditions. The computed temperature distributions are also compared in Figure 6 with those measured from the physical model. The discrepancy between the computed results and the measurements is less than 18%. Quantitative comparison between computed fluid velocities and measurements is not possible because of the difficulty in measuring low velocities in the physical model.

Figure 5 Time History of Computed Temerature Rise at Various Salient Points

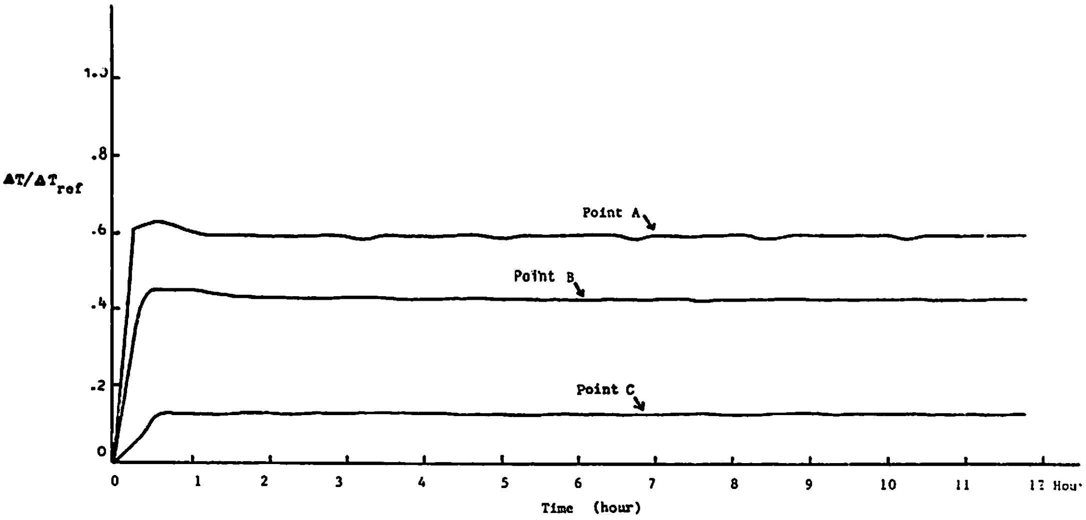

CONCLUSIONS

For the assumed operating conditions, the transition region is found to lie between radii of 0.4 km and 0.8 km measuring from the point of discharge. The temperature in this region varies roughly between 50% and 15% of the maximum temperature rise at the discharge point.

The numerical results illustrate that the vertically integrated heat transport model yields a fair degree of agreement with that of the physical model to justify its basic assumption of a vertically mixed layer.

A parametric analysis can be carried out easily using the numerical model. The studies show that the influence of the thermal diffusivity is much greater than that of the surface heat exchange coefficient in affecting the temperature distributions in the transition region. The Manning roughness coefficient does not appear to be a critical parameter in affecting the solution stability.

The study shows that lumped mass formulation yields reliable and accurate results in dynamic problems. The method is efficient and reduces computer core storage. It also permits the use of large elements as compared to that of the consistent mass representation.

REFERENCES

1. Adams, E.E., Stolzenbach, K.D. and D.R.F. Harleman : Near and far field analysis of buoyant surface discharge into large bodies of water, R.M. Pearson laboratory for water resources and hydrodynamics, Dept. of Civil Engineering, M.I.T. Technical report No.205, August, 1975.
2. Desai, C.S. and J.F. Abel : Introduction to the finite element method, A numerical method for engineering analysis, Van Nostrand Reinhold Company, 1972.
3. Kawahara, M. : The stability of the finite element stepwise integration scheme, The 24th coastal engineering seminar, Japan, 1977. (Japanese)
4. Kawahara, M. : Improved two-step Lax-Wendroff method in tidal flow analysis, The 23rd coastal engineering seminar, Japan, 1976. (Japanese)
5. Rich, L.G. : Environmental System Engineering, Mcgraw-Hill, 1973.
6. Schenck, Jr.H. : Introduction to Ocean Engineering, Mcgraw-Hill, 1975.
7. Shen, Y.Y. and R.S. McgGinnis : Thermal discharge investigation, Computer and physical modeling in hydraulic engineering, ASCE, 1980.
8. Stolzenbach, K.D. and D.R.F. Harleman : An analysis and experimental investigation of surface discharges of heated water, Technical report No.135, M.I.T. Hydrodynamics Laboratory, February, 1971.
9. Wiegel, R.L. : Oceanographical Engineering, Prentice-Hall, 1964.
10. Leendertse, J.J. : A Water-Quality Simulation Model for Well-mixed Estuaries and Coastal Seas, Vol.I, Principles of Computation, The Rand Corporation, RM-6230-RC, February, 1970.

APPENDIX-NOTATION

The following symbols are used in this paper:

C_p = specific heat of water;

E = total number of elements;

f = coriolis parameter;

Fr = Froude number;

= $V_o / (g \bar{H})^{1/2}$;

$Fr\rho$ = densimetric Froude number;

= $Vo / (g \bar{H} \Delta\rho / \rho_\infty)^{1/2}$;

g = gravitational acceleration;

h = water depth below mean sea level;

H = elevation of water surface level;

= $h + \xi$;

$\bar{H}$ = mean water depth;

H_Ω = mean water depth of an element;

K_b = friction factor;

K_x, K_y = overall thermal diffusivity;

L = differential operator;
L_x, L_y, L_z = physical model scales along the x, y and z axis;
M = total number of nodes;
n = time level;
$\overline{n}$ = unit normal vector;
Pe_x,Pe_y = Peclet number;
= $V_o\bar{H}/K_x$, $V_o\bar{H}/K_y$;
Q = discharge volume flow rate;
Re = Reynolds number;
= $V_o\bar{H}/\nu$
t = time coordinate;
T = total time of integration;
T_∞ = background water temperature;
U = vertically averaged velocity component along the x-axis;
V = vertically averaged velocity component along the y-axis;
V_o = mean discharge velocity at the point of discharge;
λ = Manning roughness coefficient;
ξ = water surface elevation above mean sea level;
ν = kinematic viscosity of water;
Ω = element domain;
ρ = water density;
ρ_∞ = water density at background water temperature;
ρ_Ω = average water density for an element;
Δ = area of a triangular element;
Δs = length of one side of a triangular element;
Δt = integration time interval;
ΔT = vertically averaged temperture rise;
ΔT_{ref} = maximum temperature rise;
Δ_ρ = difference in water density;
= $\rho - \rho_\infty$;
ϕ = surface water heat exchange coefficient;
α = artificial damping coefficient; and
β = volumetric expansion coefficient for water.